Underground Archeological Structures Detection

Anna Moudrá[1] and Michal Haindl[2(✉)]

[1] Faculty of Information Technology, Czech Technical University, 160 00 Prague, Czechia
moudrann@fit.cvut.cz

[2] The Institute of Information Theory and Automation of the Czech Academy of Sciences, 182 08 Prague, Czechia
haindl@utia.cas.cz
http://ro.utia.cas.cz/

Abstract. This paper introduces and compares three approaches for automatic archaeological heritage site detection hidden under soil cover from public aerial images. The methods use low quality public aerial RGB spectral data restricted by the land-use map to agricultural regions in the vegetation season to detect underground structures influencing plants growing on the surface soil layer.

Keywords: Remote sensing archeology · Underground heritage site recognition · Aerial image-based automated site detection

1 Introduction

Earth regions settled for thousands of years with numerous ancient cultures are rich in historical artifacts or their remains. Many of them are not visible, hidden under soil or vegetation cover for centuries. European countries are among the wealthiest archeological locations. The area of the former Bohemian kingdom, now the Czech Republic, is among them. Its location in the middle of Europe means close contact with many cultures and the site of many war conflicts that have destroyed many immovable monuments, the remains of which are often preserved only under a layer of protective soil. They are Celtic oppida, medieval fortresses, castles, gothic or baroque era fortifications, or commoners' houses.

Unless we have written historical records or other preserved references to such monuments, their discovery by archaeologists is a common question of chance. Modern remote sensing satellite or aerial sensors, however, offer tools that could significantly change this situation. It can be the ground penetrating radars or even simple spectral cameras because underneath materials influence plant growth on the surface due to locally change the subsoil layer's chemical composition and structure. The changes in vegetation coverage are caused by humidity and organic material content differences, and they appear as subtle spatial discontinuities or variations in the reflectance values (i.e., tones or colors) of vegetation and soil surface. Such features can be complemented with

K. Wojtkiewicz et al. (Eds.): ICCCI 2021, CCIS 1463, pp. 690–702, 2021.
https://doi.org/10.1007/978-3-030-88113-9_56

additional characteristics, such as the geometric pattern of the expected underground target. Fully automatic detection of hidden archeological heritage sites would be a solution to this problem. Furthermore, a reliable method would support a country-wide survey of unknown archeological sites, which is crucial for archeological heritage preservation and authorization of new construction and location development sites.

This article assumes only visible spectra, publicly available and low-quality aerial visual images, and land use maps, allowing us to process only meadows or cornfields and avoid irrelevant regions such as urban areas and forests. The rest of the paper is organized as follows: Sect. 2 briefly presents published alternatives to solve the automatic aerial heritage site detection. Section 3 explains in detail our approach and its optimization. Section 4 describes the performed validation experiments and used test data. Section 5 shows the achieved results. Section 6 summarizes the paper with a discussion and proposes some future research alternatives.

2 Related Work

For a brief history of 80 years of remote sensing application in archeology, see [5]. A more detailed overview of the European archeological remote sensing research literature can be found in [1]. The number of relevant publications is linearly growing during the reported 16 years.

Giardino [4] argues that multispectral and hyperspectral satellite data have provided important information for the discovery, delineation, and analysis of archaeological sites worldwide. Savage et al. [9] studied the application of hyperspectral (196 calibrated narrow bands in visible and shortwave infrared spectra) Hyperion satellite images for archeological applications. Although hyperspectral data are helpful to detect metallurgy production in the Faynan region of Jordan, their drawback is low spatial resolution. Zingman et al. [12,13] presents a method based on local Hough transform to detect approximately rectangular remains of livestock enclosures structures in panchromatic GeoEye1 satellite images while tolerating deviations from a perfect rectangular shape and incomplete or fragmented rectangles. High-resolution airborne hyperspectral images with 65–105 spectral bands between 400 nm and 1000 nm were used in [3] to detect remains of the Roman town of Carnuntum. They found beneficial hyperspectral imaging, especially at the beginning of the vegetation mark season or in a wet growing season. Lasaponara et al. [6] automatically detect buried archaeological remains of the UNESCO World Heritage Greek & Roman site at Hierapolis from the QuickBird-2 satellite panchromatic, multispectral bands. The rough regions are obtained by the K-means clustering followed by a supervised classifier, and the results were validated using the ground-penetrating radar. Lock and Pouncett [7] stresses the importance of GIS as the essential tools for data integration, manipulation and analysis, and spatial analysis for automatic site detection. Hidden linear ancient cultural relics visual detection from enhanced historical aerial photographs in the alluvial plain of Eastern Henan province is presented in [8]. Buried Roman archaeological remains detection in Llanera (Spain) using RGB and NIR cameras on the Unmanned Aerial Vehicle (UAV), multispectral (8 bands with 2 m resolution) WorldView-2 satellite data, and LiDAR data is investigated in [2]. They evaluate maps computed from various spectral indices. Stott et al. [10] proposes an automatic search for Viking age fortresses using airborne laser scanning data and Hough circle transformations and template matching.

Detection of archaeological sites previously occupied by farming communities in the Shashi-Limpopo Confluence Area of southern Africa from very high-resolution satellite WorldView-2 images is presented in [11]. They applied random forest and SVM classifiers to discriminate between bare soil, savannah woody vegetation, irrigated agricultural fields, archaeological sites with vitrified dung, and non-vitrified dung deposits.

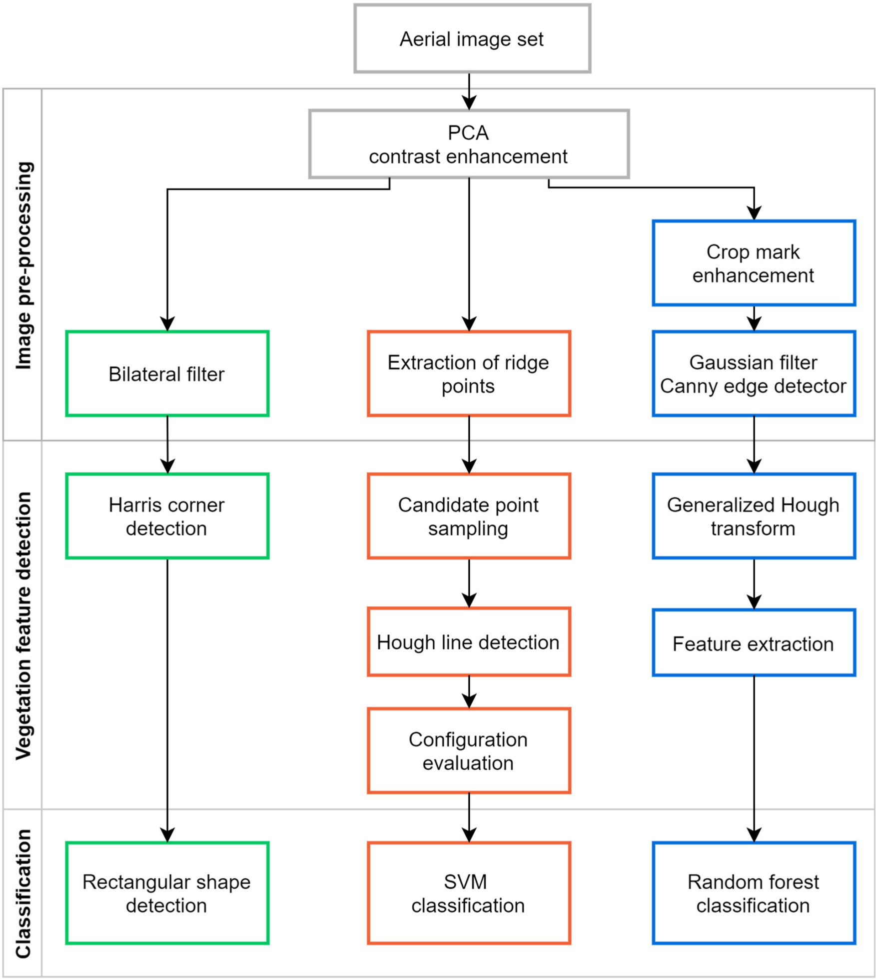

Fig. 1. The flowchart of our proposed methods. The left thread (green) represents the corner-based method (LHC/OHC), the middle thread (red) the line segment-based (RE) method, and the right thread (blue) is the template-based method. (Color figure online)

3 Proposed Approach

Three presented alternative methods together with their main functional parts are illustrated in Fig. 1. We selected the SVM and random forest classifiers to use comparable techniques standard in this application area (e.g., [11]), but the classifiers are less critical for successful archeological structures detection than the appropriate features and optimal data preprocessing.

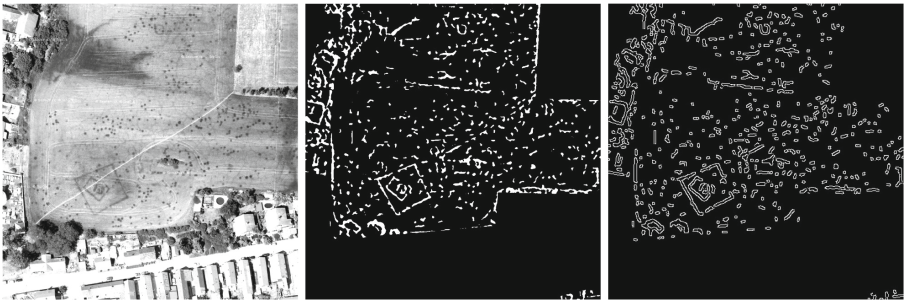

P̌C1, contrast enhanced | Enhanced image | Hough transform input

Fig. 2. Image preprocessing using the Sect. 3.3 method. Ctiněves site.

3.1 Corner Detection Based Method

Underground remains of approximately rectangular shapes can be detected using the grayscale Harris corner detector for crop mark corner extraction and subsequent geometric constraints. We propose two algorithms, each applied to a grayscale image corresponding to the first principal component of PCA applied to the original color image. Image contrast is enhanced, and a bilateral smoothing filter is applied to remove minor artifacts in our input data while preserving substantial edges. Finally, we apply the Harris corner detector to the processed, land use filtered image.

The LHC algorithm requires all four corners of a rectangular crop mark to be detected. Appropriate configurations of four corner structures, adhering to similar line length, line parallelism, and perpendicularity constraints, are considered further filtered if a line between two corners does not correspond to even a heavily fragmented edge in the original image.

In our second approach, the OHC algorithm requires finding at least three corners of an object, thus aims to overcome the issue of one undetected corner by using implicit parallelism, a similar length of these parallel lines, and the corner orientation constraint. This constraint ensures that neighboring corner orientations differ by roughly 90° moreover that the angles of corners forming a diagonal are roughly opposite.

3.2 Line Segment Based Method

The line segment-based detection referred to as the RE detection algorithm is adapted from Zingman et al., initially presented in [13] and later improved upon and reintroduced in [12]. We apply the algorithm to the grayscale, contrast-enhanced image corresponding to the first principal component (PC1) of PCA applied to the original color image. The image is prefiltered with a land-use map, a white top hat operator is applied, and the result of the operation is subtracted from the processed image to effectively suppress minor noisy artifacts such as watermarks and plough furrows. The following method, see [13], can be summarized in the following steps - black top hat operator to extract dark regions corresponding to required crop marks and other positive features in the image, thresholding, followed by morphological closing transformations, and finally, ridge extraction, is applied by selecting a point-wise maximum from morphological openings with linear structuring element of a set minimal line length at different orientations. This sequence enhances linear features in the image and suppresses background texture.

The line extraction starts with possible candidate point detection using Euclidean distance transformation, skeletonization, and candidate point sampling. Possible lines are detected using a local Hough transformation centered at each candidate point, followed by a graph construction where we consider each detected segment S, with length l, orientation θ and distance r from candidate point p_0, to be a node in a graph G. Only configurations with at least three sides, forming $\sqcup$ – like shapes and adhering to the angle and convexity constraints, see [12], are considered valid. Only the maximal cliques of each graph G we keep. The resulting rectangularity f_R (1), structure size f_S (2) measures, our proposed compactness measure f_D (3) together with the number of segments in the configuration form the feature vector used in the kernel SVM classifier.

$$f_R(G) = \Big(\sum_{S_k,S_j}^{E(G)} l_k l_j f_{90}(\beta_{k,j}) f_{cv}(\tau_{k,j}) \cdot \sum_{S_k,S_j}^{E(G)} l_k l_j f_{180}(\beta_{k,j}) f_{cv}(\tau_{k,j})\Big)^{\frac{1}{4}} , \tag{1}$$

$$f_S(G) = \frac{\sum_j l_j r_j}{\sum_j l_j} , \tag{2}$$

$$f_D(G) = \frac{2\sum_j l_j}{\sum_j dist(p_{0_j}, p_{1_j}) + dist(p_{0_j}, p_{2_j})} , \tag{3}$$

where each tuple S_k, S_j is counted only once in Eq. 1, $\beta_{k,j}$ is the angle between two line segments, $\tau_{k,j}$ is a pair-wise convexity measure, p_1, p_2 are the end point coordinates of a segment, and $dist(.)$ denotes the Euclidean distance between two points. Functions $f_{cv}(), f_{90}(), f_{180}()$ are used to weight the differences in rotation and convexity from the ideal state (segments S_k, S_j are either parallel or form a perfect corner) to the allowed angle and convexity deviation thresholds, and are further described in [12].

3.3 Template Based Method

Structures with irregular but anticipated approximately circular or rectangular shapes can be detected with the generalized Hough transform. The image preprocessing, referred to as the crop mark enhancement, is applied to the PCA-based grayscale and contrast-enhanced image. Next, the white top hat is applied to extract white noise from the image as in Sect. 3.2. Median smoothing filter, adaptive thresholding, color inversion, and erosion operator are then applied, and eventually, we discard the remaining small blob-like features. The resulting image is filtered with a binary mask of land use to retrieve only relevant regions. The Gaussian filter is applied to the crop mark enhanced image to smooth the edges of the resulting contours, and the Canny edge detector is run on the smoothed image, resulting in more continuous, flat lines.

In template matching based on generalized Hough transform, we used the perfect rectangular and circular shapes of variable sizes and wall thickness. For each region localized with the generalized Hough transform, we extracted several features. The ratio of white pixels in the localized region of the crop mark enhanced image, the overlap and difference of the enhanced image and the filled out template image, the template scale, shape, and the Hough accumulator value form a feature vector used in the random forest classifier.

4 Validation

The proposed methods have been tested on the experimental sites described in Sect. 4.1 to investigate how our method's parts are affected by the quality of available images. However, this small number of known, visually detected Bohemian archeological sites can only suggest the possible large-scale performance of the automatic underneath archeological site detection method.

4.1 Test Heritage Sites

Suggested methods were validated and mutually compared on ten unique types of sites provided by courtesy of prof. Martin Gojda. Single RGB orthorectified aerial images were acquired during the vegetation season in the 2004–2016 period. Thus they have uneven illumination and had either 0.5 or 0.25 [m] resolution. The resulting crop mark dimensions are between 54 and 279 pixels, and their wall thickness ranges from 4 to 12 pixels in each image of size 1024×1024 pixels. The set contains 7 elliptical shapes, including 5 well defined crop marks of circular shape and two significantly fragmented crop marks of elongated ellipsoids, and 7 crop marks of approximately rectangular shape. Unfortunately, this validation set is too restrictive to propose a definitive, fully automated solution, but it can suggest further investigation (Fig. 3).

- Ledčice, district Mělník (N 50° 20′0.02, E 14° 16′42.21)
- Ctiněves, district Litoměřice (N 50° 22′33.29, E 14° 18′30.77)
- Černouček, district Litoměřice (N 50° 21′24.59, E 14° 18′2.88)

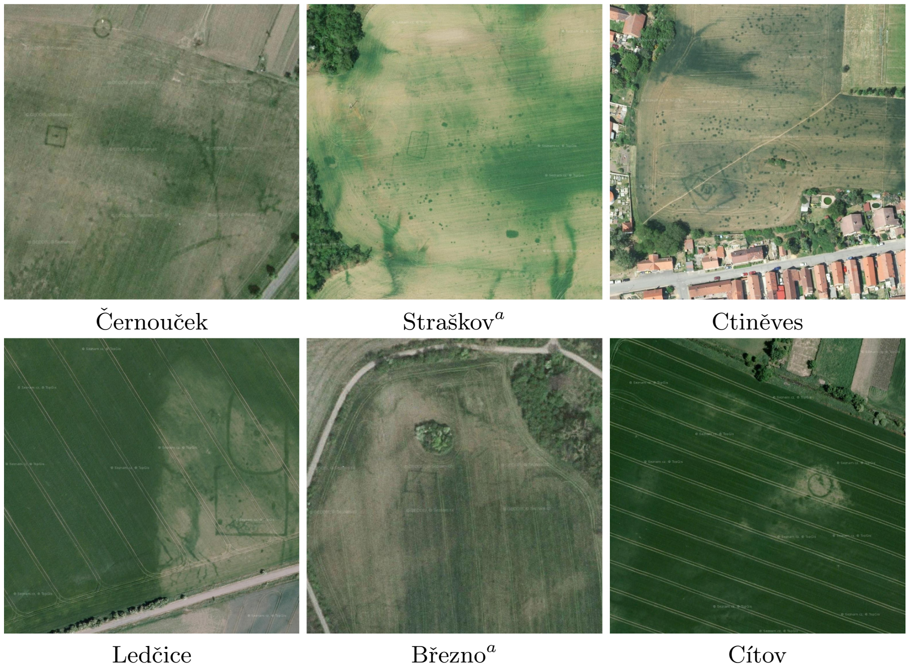

Fig. 3. Validation archeological sites.

- Straškov^{a}, district Litoměřice (N 50° 21′45.26, E 14° 15′18.77)
- Straškov^{b}, district Litoměřice (N 50° 21′55.86, E 14° 15′26.54)
- Březno^{a}, district Mladá Boleslav (N 50° 21′59.72, E 13° 45′1.73)
- Březno^{b}, district Mladá Boleslav (N 50° 22′27.57, E 13° 44′8.04)
- Cítov, district Mělník (N 50° 22′7.94, E 14° 24′7.37)
- Vražkov^{a}, district Litoměřice (N 50° 22′46.08, E 14° 15′7.65)
- Vražkov^{b}, district Litoměřice (N 50° 22′37.15, E 14° 15′51.94)

5 Results

The results achieved using the corner-based method (Sect. 3.1) tested on the single spectral first principal component images (Fig. 4). The four corners detection requirement (LHC version) was less reliable than the three corner version (OHC) because well-defined corners are sparsely present in our data. The LHC algorithm consistently detected only two crop marks[1] with one parameter setting and the OHC consistently detected three crop marks[2]. The method is susceptible to noise and extensive parameter tuning and generates many false-positive results otherwise. The minimal and maximal line length between corners was set

[1] Černouček and Ctiněves or Černouček and Březno^{b} sites.
[2] Černouček and Ctiněves and Březno^{b} sites.

Table 1. Corner-based methods: retrieval rates for most successful experimentally found parameter setting.

Algorithm	FP	TP
LHC	20	2
OHC	3	3

Table 2. Template-based method: retrieval rates with all features included.

Template type	τ	FP	TP
Rectangular	1.1	3	7
Circular	0.8	22	6

to 30 and 240 pixels for the LHC method. The maximum allowed deviation from line parallelism was set 25° and at 15° for deviation from line perpendicularity. At least 60% of an edge between two corners must be intact for a line to be considered valid. In the OHC algorithm, the minimal and maximal line length between corners was set to 30 and 270 pixels, and the maximum allowed deviation of corner orientation from the orientation of the presumed diagonal was set at 30°, as it is understood that more elongated rectangles may deviate more. The maximum allowed deviation for line perpendicularity was set at 20°. At least 85% of an edge between two corners must be intact. From our testings, the constraint placed on the completeness of the two adjacent edges was very effective in reducing false positives. The frequent limitation of the corner-based method is remaining irrelevant structures such as trees or furrows—this method requires sophisticated pre and post-processing to decrease the amount of retrieved false positives. The OHC version performs slightly better than LHC, results shown in Table 1, but the detected corner orientation precision requires further improvement. Of the three approaches, this method was the worst-performing on the tested images. From the site examples with rectangular crop marks only correct results are Černouček, Ctiněves, and Březno^b shown in Fig. 4. The remaining pictured results containing high number of false-positives are more typical for this method, as Harris corner detection results in many redundant salient points, generating rectangular configurations that remain unfiltered by the algorithms.

The line segment based method (Sect. 3.2) used in the pre-processing steps the white top hat square SE size 4×4 pixels, the black top hat was applied with square SE of size 15×15 pixels. The pixels with an intensity lower than 20 are suppressed to 0 with thresholding. The morphological closing square size SEs were set to 2×2 pixels for dilation and 3×3 pixels for erosion. The MFC operator was applied with structuring elements of size 3×3 and 10×10 pixels. The linear segments were enhanced by the composite opening with linear SE set to 30 pixels and rotated in increments of 5° the threshold set for valid ridge extraction was set to 60. The candidate points were sampled with the sampling rate five, and the window multiplier parameter was set to 1.8 see [12], all candidate points having a distance smaller than ten or greater than 170 pixels were discarded. The minimum line length for the line segment extraction was set to 20 pixels. The threshold values for angle constraint applied to $\beta_{k,j}$ is set to 15° and the convexity constraint $\tau_{k,j}$ threshold is 0.4.

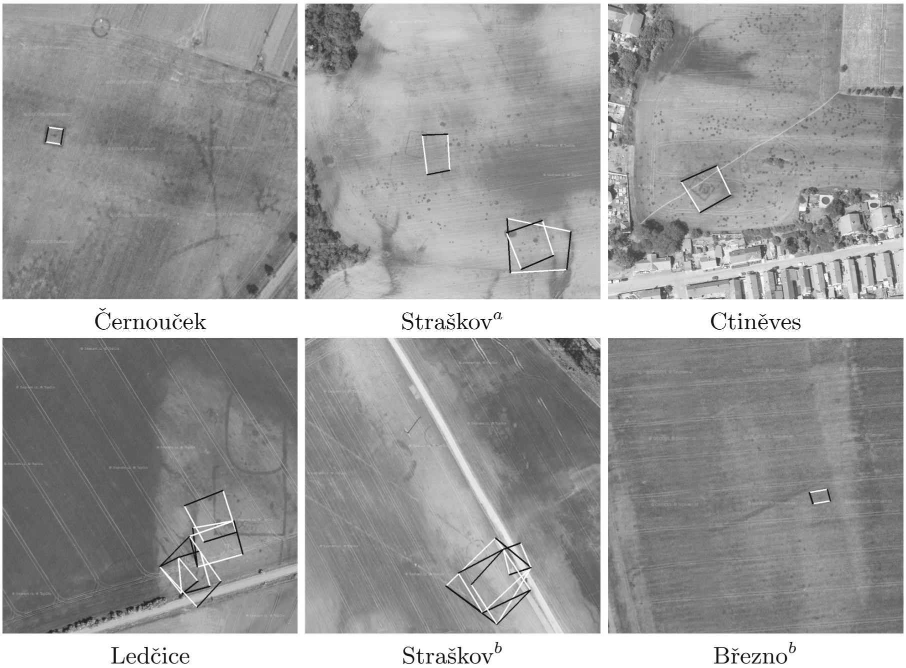

Fig. 4. Detected rectangular shapes using the Sect. 3.1 method.

Similar to [12], the method was evaluated based on the feature's ability to discriminate crop marks from irrelevant structures. We conducted this experiment by setting the parameter class weight on the SVM classifier, and results are included in Table 3. The results include some duplicity due to candidate point oversampling for significant crop marks, the unique true positives denoted as TP_u. Overall, the RE method successfully detected all seven unique rectangular crop marks across our validation data.

The methods limiting factor is its high sensitivity to noise. We encountered significantly more noise in the processed data than the original paper [12] suggested, perhaps as a result of arable land photographed at high resolution containing many more linear structures such as furrows than the original satellite data. Our modification of the original RE method, the introduced compactness measure, according to our validation, improved the ability to discriminate irrelevant structures further. However, additional improvements are needed. Another limitation of the RE method is its inability to generalize detection for other shapes than imperfect rectangles.

The template-based method (Sect. 3.3) uses in the pre-processing steps the following experimentally found parameters. First, the white top hat is square SE is set to size 4×4 pixels. Next, a median filter is applied with kernel size 5×5 pixels. Adaptive threshold of size 37×37 pixels and constant $C = 7$ is used, and the then inverted image is eroded with square SE of 2×2 pixels. Finally,

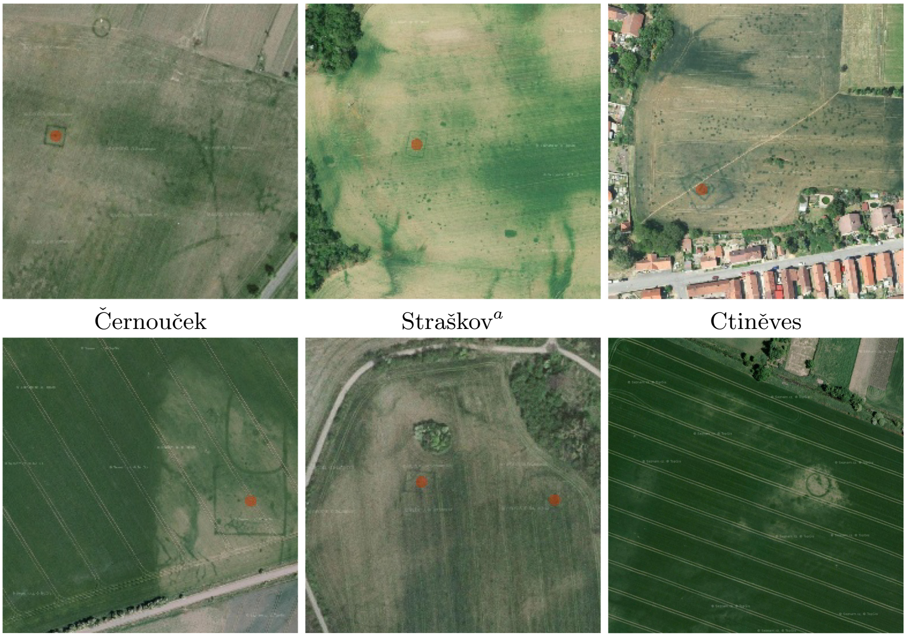

Černouček | Straškov[a] | Ctiněves

Ledčice | Březno[a] | Cítov

Fig. 5. Detected rectangular shapes using the Sect. 3.3 method.

blobs with an area smaller than 50 pixels are removed. Then, the crop mark enhanced image is smoothed with Gaussian filter kernel of size 9×9 pixels, and $\sigma = 1.6$ the Canny edge detector is applied with Sobel operator size set to 3×3 pixels and the lower and upper hysteresis thresholds are set to 40 and 70. The constitutive steps of pre-processing are shown in Fig. 2.

Table 3. RE: retrieval rates with all features included.

			(f_R, f_S, f_D)		(f_R, f_S)		
Dataset	Class_weight	FP	TP	TP_u	FP	TP	TP_u
PC1	0.99	16	18	7	30	18	7
PC1	0.98	1	16	7	15	15	7
PC1	0.95	0	10	6	4	13	6

We experimented with double-edged templates of rectangular and circular shapes. For the rectangular templates, the side length ratios were set to $\{0.6, 0.7, 0.8, 0.9, 1.0\}$. The rectangular shapes were rotated in three degrees steps size in the range $\langle 0°, 180° \rangle$, and the width between the template edges is set to be between 4 and 6 pixels. The total number of scales between the maximum

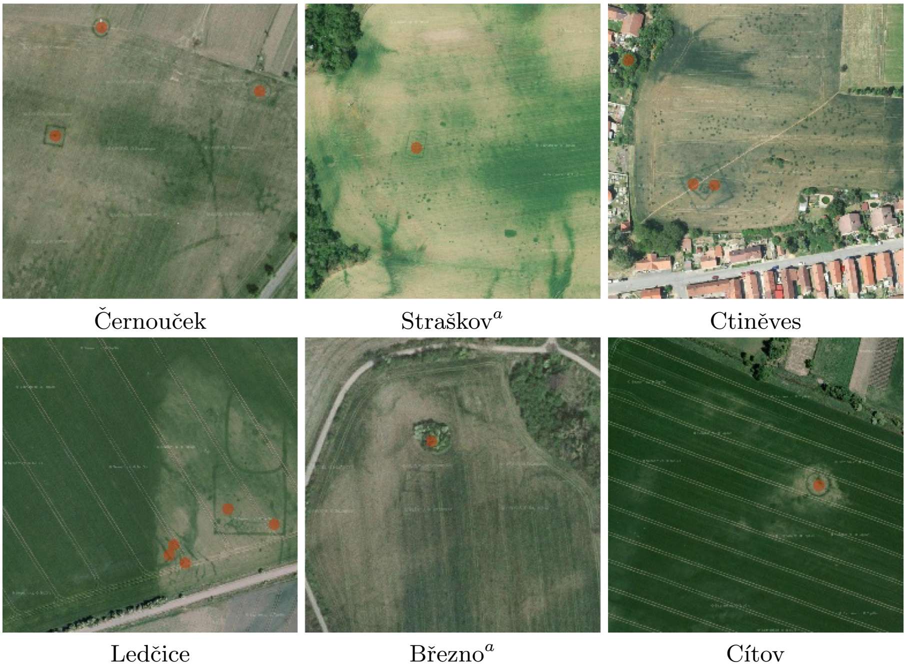

Fig. 6. Detected circular shapes using the Sect. 3.3 method.

and minimum template dimensions was set to 40 for both template types. The Hough transform threshold influences the precision-recall trade-off. Our goal was to retrieve as many crop marks as possible while allowing for a higher rate of false positives to be retrieved and later filtered out in the classification stage. Eventually, we set the value threshold value $\tau = 1.1$ for rectangular template shapes. For circular shapes, $\tau = 1.0$ proved to be a good value for crop marks that were almost entirely intact, like the two in site Černouček. The threshold needed to be lowered to 0.8 to retrieve fragmented shapes like the one in Vražkov^b. The random forest classifier was trained with 50 estimators with a maximum depth set to 3 and a class weight parameter set to 0.98. Eventually, we trained the model for each template type separately, as mixing the two led to significantly worse results.

The template-based algorithm is by a significant margin the most successful method, with seven rectangular and six circular crop marks detected and only a limited number of false positives, included in Table 2. Figure 5 illustrates the rectangular detection results with one erroneous detection on the Březno^a image while correctly missing any false negative on the Cítov image. The circular template results in Fig. 6 are worse, as the Hough transformation with a lower threshold retrieves substantially more false positives. Černouček site has two correct detections and one wrong; Straškov^a, Ctiněves, and Ledčice have false positives, and only Březno[a] and Cítov contain correct results. However, many circular erroneous results are true archeological sites but with rectangular shapes.

The significant advantage of the template-based approach is its capability to generalize to a wider variety of shapes. Our validation experiment shows that a lack of prior knowledge of a detected crop mark's exact shape and size can be compensated for with a more extensive template set. However, this approach inevitably leads to increased computational complexity, which needs to be further mitigated with parallelization.

6 Conclusions

We present the algorithms for automatic archaeological heritage recognition hidden under the soil cover from aerial images. Three alternative methods can detect underground remains of buildings or other construction artifacts based on vegetation cover changes due to locally changed the subsoil layer's chemical composition and structure. As such, they have the potential to significantly speed up the complex and time-consuming visual detection of aerial photographs. Despite this restriction, these methods can assist in hidden archeological or construction site detections and impact the cataloging of the hitherto unknown archaeological sites.

The performance quality of the algorithms was mutually compared, verified, and demonstrated on the ten known, visually detected Bohemian archeological sites. The generalized Hough transform-based method is the most versatile and reliable approach to detect hidden archeological or construction sites belowground, provided they are not occluded by modern structures above. Multimodal and better quality data, combined with radar satellite images, interferometry, and lidar, could significantly improve detection results. Although new multispectral and high-resolution remote sensors acquire the ever-growing amount of high-quality information from a distance, the weak point is the ground truth verification of the results for calibration of the instruments or improvements of existing algorithms.

Acknowledgments. The Czech Science Foundation project GAČR 19-12340S supported this research. The archeological sites suggestion was provided by courtesy of prof. Martin Gojda from the Institute of Archaeology of the Czech Academy of Sciences, Prague.

References

1. Agapiou, A., Lysandrou, V.: Remote sensing archaeology: tracking and mapping evolution in european scientific literature from 1999 to 2015. J. Archaeol. Sci. Rep. **4**, 192–200 (2015). https://doi.org/10.1016/j.jasrep.2015.09.010
2. Calleja, J.F., et al.: Detection of buried archaeological remains with the combined use of satellite multispectral data and UAV data. Int. J. Appl. Earth Obs. Geoinf. **73**, 555–573 (2018)

3. Doneus, M., Verhoeven, G., Atzberger, C., Wess, M., Ruš, M.: New ways to extract archaeological information from hyperspectral pixels. J. Archaeol. Sci. **52**, 84–96 (2014). https://doi.org/10.1016/j.jas.2014.08.023
4. Giardino, M.J.: A history of nasa remote sensing contributions to archaeology. J. Archaeol. Sci. **38**(9), 2003–2009 (2011). https://doi.org/10.1016/j.jas.2010.09.017. Satellite remote sensing in archaeology: past, present and future perspectives
5. Kucukkaya, A.G.: Photogrammetry and remote sensing in archeology. J. Quant. Spectrosc. Radiat. Transf. **88**(1–3), 83–88 (2004)
6. Lasaponara, R., Leucci, G., Masini, N., Persico, R., Scardozzi, G.: Towards an operative use of remote sensing for exploring the past using satellite data: the case study of hierapolis (Turkey). Remote Sens. Environ. **174**, 148–164 (2016). https://doi.org/10.1016/j.rse.2015.12.016
7. Lock, G., Pouncett, J.: Spatial thinking in archaeology: Is GIS the answer? J. Archaeol. Sci. **84**, 129–135 (2017). https://doi.org/10.1016/j.jas.2017.06.002. Archaeological GIS Today: Persistent Challenges, Pushing Old Boundaries, and Exploring New Horizons
8. Lu, P., et al.: On the use of historical archive of aerial photographs for the discovery and interpretation of ancient hidden linear cultural relics in the alluvial plain of eastern henan, china. J. Cult. Heritage **23**, 20–27 (2017). https://doi.org/10.1016/j.culher.2015.09.010. Beyond the modern landscape: Earth Observation to see the unseen
9. Savage, S.H., Levy, T.E., Jones, I.W.: Prospects and problems in the use of hyperspectral imagery for archaeological remote sensing: a case study from the Faynan copper mining district, Jordan. J. Archaeol. Sci. **39**(2), 407–420 (2012). https://doi.org/10.1016/j.jas.2011.09.028
10. Stott, D., Kristiansen, S.M., Sindbæk, S.M.: Searching for Viking age fortresses with automatic landscape classification and feature detection. Remote Sens. **11**(16), 1881 (2019). https://doi.org/10.3390/rs11161881
11. Thabeng, O.L., Merlo, S., Adam, E.: High-resolution remote sensing and advanced classification techniques for the prospection of archaeological sites' markers: the case of dung deposits in the Shashi-Limpopo confluence area (Southern Africa). J. Archaeol. Sci. **102**, 48–60 (2019)
12. Zingman, I., Saupe, D., Penatti, O.A.B., Lambers, K.: Detection of fragmented rectangular enclosures in very high resolution remote sensing images. IEEE Trans. Geosci. Remote Sens. **54**(8), 4580–4593 (2016). https://doi.org/10.1109/TGRS.2016.2545919
13. Zingman, I., Saupe, D., Lambers, K.: Automated search for livestock enclosures of rectangular shape in remotely sensed imagery. In: Image and Signal Processing for Remote Sensing XIX, vol. 8892, p. 88920F. International Society for Optics and Photonics (2013)